Originally published as:

Christoph Limbach, Michael M. Laue, Xiaolu Wang, Bin Hu, Nadine Thiede, Greta Hultqvist, and Manfred W. Kilimann.
Molecular in situ topology of Aczonin/Piccolo and associated proteins at the mammalian neurotransmitter release site.
(2011) Proceedings of the National Academy of Sciences of the United States of America, 108 (31), pp. 392-401.

DOI: 10.1073/pnas.1101707108

Molecular in situ topology of Aczonin/Piccolo and associated proteins at the mammalian neurotransmitter release site

Christoph Limbach,[a] Michael M. Laue,[b,1] Xiaolu Wang,[b,2] Bin Hu,[b] Nadine Thiede,[a] Greta Hultqvist,[a] and Manfred W. Kilimann[a,b,3]

[a]*Department of Neuroscience, Uppsala University, S-75124 Uppsala, Sweden; and*
[b]*Institut für Physiologische Chemie, Ruhr-Universität Bochum, D-44780 Bochum, Germany*

Abstract

*The protein machinery of neurotransmitter exocytosis requires efficient orchestration in space and time, for speed and precision of neurotransmission and also for synaptic ontogeny and plasticity. However, its spatial organization in situ is virtually unknown. Aczonin/Piccolo is a putative organizer protein of mammalian active zones. We determined by immunogold electron microscopy (EM) (*i*) the spatial arrangement (i.e., topology) of 11 segments of the Aczonin polypeptide in situ, and correlated it to (*ii*) the positioning of Aczonin-interacting domains of Bassoon, CAST/ELKS, Munc13, and RIM and (*iii*) the ultrastructurally defined presynaptic macromolecular aggregates known as dense projections and synaptic ribbons. At conventional synapses, Aczonin assumes a compact molecular topology within a layer 35 to 80 nm parallel to the plasma membrane (PM), with a "trunk" sitting on the dense projection top and a C-terminal "arm" extending down toward the PM and sideward to the dense projection periphery. At ribbon synapses, Aczonin occupies the whole ribbon area. Bassoon colocalizes with Aczonin at conventional synapses but not at ribbon synapses. At both conventional and ribbon synapses, CAST, Munc13, and RIM are segregated from Aczonin, closer to the PM, and Aczonin is positioned such that it may control the access of neurotransmitter vesicles to the fusion site.*

Neurotransmitter release is confined to a specialized area of the presynaptic plasma membrane (PM) known as the active zone. Calcium-dependent exocytosis at the synapse is an elaborate, multistep process that is fast and precise, yet highly restrained and subject to modulation (i.e., presynaptic plasticity) (1). A solubilization-resistant lattice of proteins associated with the inner face of the presynaptic PM, the cytomatrix at the active zone (CAZ), is apparent on electron microscopy (EM) imaging and seems to integrate and organize many proteins of the presynaptic machinery (2).

When mammalian conventional synapses are stained with heavy metal ions, EM reveals regularly spaced, cone-shaped structures of a size of approximately 50 nm attached to the presynaptic PM, which are known as dense projections (DPs) or, collectively, the "presynaptic particle web" or "presynaptic grid." It has been possible to isolate DP-like particles by subcellular fractionation, and even to reconstitute similar aggregates after previous solubilization, and many proteins of the presynaptic molecular machinery have been detected in them (3). These findings suggest that the presynaptic machinery may be organized into modular units of homogeneous size and shape, and possibly also of defined stoichiometry and spatial organization of its constituent proteins. An organized positioning of individual proteins and protein domains could allow these supramolecular assemblies to function as "molecular machines" and contribute to the high speed, precision, and fine-tuning that is characteristic for synaptic exocytosis. Morphological organization of active zone material into distinctive electron-dense bodies has, in fact, been observed in many synapse types and species. Examples of particularly striking morphology are the T-bars of various *Drosophila* synapses and the ribbons of vertebrate sensory synapses (4).

Several families of multidomain proteins have been identified that seem to contribute to the supramolecular organization of the active zone: CAST/ELKS, liprin-α, Munc13, and RIM. In vertebrates, the related giant proteins Aczonin/Piccolo (550 kDa) and Bassoon (420 kDa) may serve

as scaffolds for the organized assembly of individual DPs and/or of the presynaptic particle web as a whole. Molecular studies have revealed that these and additional proteins are multiply interconnected, further strengthening the notion of a highly integrated supramolecular assembly of active zone proteins (refs. 2, 5 and references therein). However, although many, if not most, of the proteins participating in neurotransmitter vesicle dynamics have been identified and the characterization of individual molecular interactions between them proceeds, very little is known about how the mechanistic cooperation of these proteins is organized in space and time.

Multidomain proteins as large as Aczonin and Bassoon may have considerable structural flexibility, particularly in the linker segments between domains, and their overall topology (the relative spatial positioning of their domains) may be substantially influenced by their interaction partners. Of foremost interest is, therefore, not their molecular topology as individual proteins in solution, but in their supramolecular context in situ, at their presynaptic site of action. In the present study, we undertook to bridge the gap between the molecular and ultrastructural characterization of the neurotransmitter release site. By immunogold EM, we investigated in conventional and ribbon synapses (*i*) the molecular in situ topology of multiple segments of the long Aczonin polypeptide and correlated it to (*ii*) the positioning of selected domains of other active zone proteins and (*iii*) the ultrastructurally defined presynaptic macromolecular aggregates known as DPs and synaptic ribbons.

Results

Stratified Localization of Aczonin and Its Interactor Proteins Within Two Vesicle Diameters from Presynaptic PM of Conventional Synapses.

The linear dimensions of the Aczonin and Bassoon polypeptide chains are in the same order of magnitude as the diameter of a typical neuroneuronal synaptic terminal. At the extreme, if it were an extended α-helix, Aczonin could stretch across approximately 750 nm, or approximately 20 vesicle diameters. More plausibly, it might resemble a string of beads with well folded domains separated by poorly structured, flexible linkers. This has invited the assumption that Aczonin and Bassoon might reach, filament-like, from the presynaptic PM into the depth of the terminal, serving as tethers and conducting vesicles from the reserve pool toward the fusion site (6–8). However, data on the actual arrangement of these giant protein molecules in situ, at the active zone, have been lacking.

We generated antibodies against a series of 11 partial sequences along the Aczonin polypeptide chain (Fig. 1*A* and Table 1), and determined the distances of the respective segments of holo-Aczonin from the presynaptic PM, by preembedding immunogold EM in the molecular layer of perfusion-fixed rat brain cerebellum (Fig. 1). Most synapses in this area are excitatory parallel fiber synapses. Individual sequence segments were detected at circumscript PM distances, the more sensitive antibodies producing striking narrow stripes of immunodecoration particles (Fig. 1*B*). Remarkably, Aczonin was not found to reach deeply into the terminal. Instead, the immunogen sequences were grouped in three distinct layers parallel to the presynaptic PM at a maximum distance of 79 nm. The epitopes within the N-terminal 70% of the Aczonin sequence were localized in two zones at 73 to 79 nm (immunogens AczN, Acz2, Acz4) and 57 to 61 nm (Aczp2p4, Acz3, Aczp18p19) from the PM (Fig. 1*C*), whereas the epitopes in the C-terminal 30% of the sequence (Acz6, Acz7-6, Acz8, AczC2A, AczC2) were mapped significantly closer to the PM (pairwise Kolmogorov–Smirnoff test, $P < 0.001$) at distances of 33 to 39 nm (Fig. 1*D*).

The C-terminal sequence region includes the third coiled-coil (CC3) domain of Aczonin (construct Acz7-6) which binds to CAST1, Munc13-1 and, indirectly via the Munc13-1 N-terminal (NT) domain, Bassoon and RIM1 (5). We therefore also investigated the localizations of the respective binding partner domains. Antibodies against three immunogens representing the Bassoon C-terminal (CT) region (two of them nonoverlapping; Table 1) labeled PM distances of 35 to 37 nm (Fig. 1*E*), in excellent agreement with each other and with the Acz7-6 localization (37 nm). In contrast, the NT regions of Munc13 (detected by two independent sera against immunogen construct, Mu1) and RIM (detected by three independent sera against immunogen construct, Rim43) were localized significantly closer ($P < 0.001$) to the PM at a distance of 19 nm (Fig. 1*F*). Characterization of the isoform specificities of the Mu1 and Rim43 antibodies, which were raised against NT sequences of Munc13-1 and RIM1α (Fig. 1*A* and Table 1) but cross-react also with homologous sequences of, respectively, ubMunc13-2 (10–30% relative sensitivity) and RIM2α (25–40% relative sensitivity) is described in *SI*

Results and Fig. S1. The localizations of the Munc13 and RIM NT sequences coincide with that of a peptide epitope in the large central cytoplasmic loop of the α1A subunit of the $Ca_v2.1$ (P/Q-type) Ca^{2+} channel (20 nm; Fig. 1*G*). We did not obtain an immunolocalization signal with the antisera that we raised against the central region of CAST1 (construct Cast3; Table 1), presumably because CAST1 is not expressed in the cerebellum (9).

The distance of the N-terminal and central regions of Aczonin from the presynaptic PM is similar to the vertical size of DPs (~50 nm), and the PM distance of the C-terminal regions of Aczonin and Bassoon is similar to the diameter of neurotransmitter vesicles (~35–40 nm). We applied a uranyl acetate/methyl cellulose adsorptive staining (10) to visualize the DPs in Lowicryl K4M sections (Fig. 1*H*). When combining DP staining and postembedding immunodecoration of the Aczonin region Aczp18p19, the median PM distance of the gold particles in molecular layer synapses (55 nm; *SI Results* provides details) was in accordance with the value determined earlier by preembedding immunolabeling (59 nm), and slightly larger than the median height of DPs, which we determined in our specimens as having a median value of 45 nm [95% confidence interval (CI), 42–48; $n = 110$]. The DP width at the base was determined as having a median value of 56 nm (95% CI, 50–61; $n = 110$), and the DP distance, center to center, as having a median value of 72 nm (95% CI, 67–78; $n = 86$). These data confirm by costaining in the same specimen that Aczp18p19 localizes closely above the tips of DPs. Additional validation of the morphometric results under a variety of technical parameters is described in *SI Results*.

Lateral Topology of Aczonin and Its Interactor Protein Domains Relative to DPs.

Postembedding immunolabeling of Aczonin sequence p18p19 and costaining of DPs indicated a localization of this part of the Aczonin molecule slightly above the tips of DPs, not only in the vertical direction (perpendicular to the PM) but also laterally (Fig. 1*H*). This impression was confirmed by statistical analysis of postembedding labeling with antibodies against Acz2, Aczp18p19, and Acz3, which consistently gave distributions centering on the DP tips.

As postembedding labeling was successful with only a minority of antibodies, we subsequently applied preembedding immunolabeling, before which DPs were visualized by ethanolic phosphotungstic acid (EPTA) staining (11). Lateral distances of immunolabel particles to the nearest DP were measured, and the following considerations were applied to evaluate the lateral distributions at DPs (Fig. 2). Four unimodal (Fig. 2*A*) and six bimodal distributions (Fig. 2 *B* and *C*) were obtained, all virtually left/right symmetric with median values close to zero (Table 2; bilateral evaluation; mean median value of all 10 immunogens, 1.2 nm). Every structural determinant of Aczonin must have a finite true distance from the DP axis, and if particle localizations are discriminated by “left” (minus) and “right” (plus) as in the column diagrams of Fig. 2, bimodal distributions are in principle always expected. However, if the true lateral distance is smaller than the scatter of the immunodetection technique (approximately ±10 nm), the two peaks will be blurred into one. If the true lateral distance is larger than this scatter, a bimodal distribution will be seen. As the distributions were left/right symmetric, data were analyzed further after pooling the left and right wings of the distributions by deleting the algebraic “minus” signs (unilateral evaluation; Table 2). For the six bimodal distributions, the resulting medians (M*) and 95% CIs give a measure of the true lateral positions of the respective aa sequences and their accuracies, respectively. For the four monomodal distributions, the median values (M* = 14–15) mainly reflect the inaccuracy of the detection technique, with additional contributions of true lateral localizations of the respective immunogens that cannot be quantified but probably are no greater than 5 nm. The peak widths of the bimodal distributions (average 95% CI, 4 nm) are expected to reflect the technical inaccuracy only, whereas both technical inaccuracy and true lateral displacement of the immunogen are expected to contribute to the broader peak widths of the monomodal distributions (average 95% CI, 7 nm; Table 2).

Strikingly, the lateral localizations of Aczonin sequences were categorized into two groups that correlate with their vertical localizations (Fig. 2 *A* and *B*). The lateral localizations of AczN, Acz2, Aczp18p19, and Acz3 were close to the DP axis (vertically, these immunogens localize 57–79 nm from the PM), whereas Acz8, AczC2A, and AczC2 (vertical PM distances, 33–39 nm) localized toward the periphery of DPs. Whereas the most C-terminal immunogens, AczC2A, and AczC2 (both, M* = 22 nm) approach the middle of DP intervals (median 36 nm), the more N-terminal sequence Acz8 lies closer ($P < 0.05$) to the DP center (M* = 16 nm). The CT region of Bassoon (BsnH12-3; M* = 18) and

the NT regions of Munc13-1/ubMunc13-2 (Mu1; M* = 23) and RIM1/2α (Rim43; M* = 22) also localized to the periphery of DPs, BsnH12-3 colocalizing laterally with Acz8 ($P < 0.05$) and Mu1/Rim43 with AczC2A/C2 ($P < 0.05$; Fig. 2*C*). We did not obtain immunolocalizations in this preparation with antibodies against Aczp2p4, Acz4, Acz6, Acz7-6, CAST1, and Ca^{2+} channel.

The differential vertical localizations of the N-terminal Aczonin regions (PM-distal) versus the C-terminal Aczonin regions and Bassoon-CT, Munc13-NT, and RIM-NT (PM-near; Fig. 1) were qualitatively confirmed in this preparation (Fig. 2 *A*–*C*, *Top*), but not quantified because of the poorer structure preservation. Also in PM-parallel sections, anti-Rim43 immunolabeling localized to the sides of DPs (Fig. 2*D*), whereas oblique sections confirmed anti-Aczp18p19 immunolabeling to lie above the DP layer (Fig. 2*E*).

Topology of Aczonin and Its Interaction Partners at Photoreceptor Synaptic Ribbons.

The aforementioned results argued for a compact topology of the Aczonin polypeptide at conventional synapses. To complement these data, we performed preembedding immunolabeling of perfusion-fixed rat retinal photoreceptor (mostly rod) synapses. The presynaptic ribbons of these specialized synapses are striking, sharply demarcated dense structures of very uniform morphology that are EM-visible without the heavy metal staining required to visualize conventional DPs.

Immunolabeling was obtained with antibodies against nine of the 11 Aczonin immunogens. The most sensitive antibodies, like anti-Aczp18p19 (Fig. 3*A*), decorated the whole extent of ribbons in vertical (Fig. 3*A*, *Left*) and horizontal sections (Fig. 3*A*, *Middle*), as well as of round structures (Fig. 3*A*, *Right*) that probably are ribbon precursor spheres implicated in the structural plasticity of ribbon synapses (12). The vast majority of particles was observed at or close to the ribbon surface within a distance of twice the ribbon width (~40 nm), corresponding to the interval between the ribbon and the row of vesicles tethered to it (Fig. 3*A*, *Middle*). Particles were rarely found inside the ribbon matrix. For morphometry, we determined the lateral distance of the immunolabel from the ribbon surface and the vertical distance from the PM at the synaptic ridge. To compensate the variation in ribbon dimensions, the lateral distance of each particle was normalized to the ribbon width, and the vertical distance was normalized to the distance between ribbon tip and PM ridge, of the respective synapse. The ribbon width determined in cross sections running through the center of photoreceptor ribbon synapses was 21.7 nm ± 3.7 nm (mean ± SD; $n = 420$). By measuring the distance between ribbon tip and PM (257 nm ± 66 nm; $n = 420$) and the distance between ribbon base and PM (57 nm ± 12 nm; $n = 324$), we calculated a mean ribbon height of 200 nm.

The distribution patterns of all Aczonin immunogens, regardless of their differential localizations at conventional synapses, were indiscriminable in both directions, perpendicular to and along the ribbon axis. Median distances from the ribbon surface ranged from 10.4 nm (AczC2) to 23.4 nm (Aczp2p4), and median distances normalized to ribbon widths were between 0.46 (Acz3) and 0.96 (Acz7-6; Table S1). Distinct layers of immunogen localization as at conventional synapses were not observed. Along the vertical ribbon axis (perpendicular to the PM), Aczonin immunogens exhibited broad distributions that did not appear to differ significantly from each other (Fig. 3*B*), with median relative values in a range between 0.63 (Acz2, AczC2) and 0.77 (Acz8; Table S1). Aczonin labeling reached down to the ribbon base, sparing the arciform density and the vicinity of the PM.

Immunolabeling against CtBP2/Ribeye, a scaffold protein and molecular marker of ribbons, also lined the ribbon surface, with lateral and vertical distributions indiscriminable from those of the Aczonin immunogens (Fig. 3*B* and Table S1), but spared the ribbon's electron-dense cross-section, as did all other labelings. This suggests that the preembedding detection system did not penetrate the ribbon matrix.

All other immunogens (the CT region of Bassoon, the NT regions of Munc13-1/ubMunc13-2 and of RIM1/2α, and the central region of CAST1) were found in a location complementary to that of Aczonin and Ribeye, near the base of the ribbon and the putative vesicle fusion site (which is presumed to be at the rim of the presynaptic PM groove). Median relative PM distances along the ribbon axis were 0.25 for Rim43, 0.29 for Cast3, 0.35 for BsnH12, and 0.41 for Mu1, all indistinguishable (PM ridge, 0; ribbon tip, 1; ribbon base, 0.23 ± 0.05; Fig. 3*C* and Table S1). Particle distributions perpendicular to the ribbon axis were indistinguishable among all immunogens investigated.

Discussion

Dense Projections: Fact or Artifact?

The demonstration of DPs by heavy metal impregnation of chemically fixed EM specimens (11)—supported by the biochemical purification, differential solubilization, and even reconstitution of DP-like particles (3)—suggested that the molecular machinery of presynaptic active zones may be organized into repetitive modular units of regular size, shape, and spacing. A unifying view sees the aggregation of presynaptic proteins into different types of "dense bodies" as a universal feature of the molecular architecture of active zones, merely differing in degrees of order, compaction, and morphological, functional, molecular, or phylogenic diversification (4). Electron tomography of chemically fixed conventional synapses described an organization of active zone material into a regular array of polyhedral cages ("syndesomes") approximately 60 nm in diameter (13). A different type of regular structuring of active zone material ("ribs and beams") has been characterized by electron tomography of chemically fixed neuromuscular junctions of frog and mouse (14, 15).

Electron tomography of cryofixed conventional rodent synapses, processed by cryosubstitution and embedding (16, 17) or by direct cryoelectron tomography of the frozen/hydrated specimens (18), did not detect DP- or syndesome-like aggregates of the presynaptic cytomatrix, but, instead, a more diffuse network of filaments similar to the findings of older quick-freeze deep-etching studies (19–21). In these studies, it is proposed that chemical fixation gives rise to DPs by causing the collapse of protein filaments. However, we do not believe that DPs are "mere artifacts," but suspect that the truth lies between the extremes of "fact" and "artifact." The regular size and spacing of DPs in classical transmission EM, the elaborate ultrastructure of the syndesomes (13), the biochemical purification and reconstitution of DP-like aggregates (3), and also the defined and differential localizations of domains of Aczonin, Bassoon, Munc13, and RIM relative to DPs in our present study, all suggest that the CAZ of conventional synapses possesses an intrinsic molecular pattern. This pattern may well be looser and more flexible in the native state, being compacted to some degree by chemical cross-linking and highlighted by heavy metal staining (22). T-bars of *Drosophila* neuromuscular synapses were characterized after either chemical fixation or cryofixation in the same study (23), and found to be 20% to 30% taller and wider in the cryofixed specimens but to have similar shapes, including filamentous protrusions at their distal ends, in both preparations. We therefore believe that DPs do reflect an underlying organization of the active zone material into modules of defined size, shape, and molecular architecture, even though their exact ultrastructural appearance and quantitative parameters may be influenced by the technique of specimen processing.

Aczonin Has a Compact in Situ Topology at Conventional and Ribbon Synapses.

Fig. 4 graphically summarizes the localizations of the different protein regions determined in our study at conventional synapses (Figs. 1 and and2)2) and correlates them with the dimensions of neurotransmitter vesicles and DPs. In the vertical direction, the entire Aczonin polypeptide chain is detected within a layer 33 to 79 nm parallel to the PM, with the N-terminal 70% and the C-terminal 30% of the sequence confined to even narrower layers of 57 to 79 nm and 33 to 39 nm, respectively.

Differential localizations were also found in the horizontal direction, relative to DPs: whereas segments of the N-terminal major part of the polypeptide localize close to the DP axis, epitopes in the C-terminal minor part were detected at the DP periphery. The AczN, Acz2, Aczp18p19, and Acz3 antibodies gave monomodal label distributions with maxima over the DP axis, indicating that their main epitopes are closer to this axis than the resolution of the detection system (approximately ±10 nm). In contrast, the lateral displacement of Acz8 and BsnH12-3 labeling was large enough to produce two clearly separated maxima (Fig. 2). The remaining antibodies (AczC2A, AczC2, Rim43, Mu1) detected immunogen localizations even further toward the DP periphery. Our transmission EM technique is expected to produce lateral localizations that are systematically too small, closer to the DP axis than the true epitope localizations, because it gives 2D projections of 3D particle distributions. In sections approximately 70 nm thick, enclosing rows of several DPs (56 nm wide), most immunolabel particles will lie at angles to the section plane (Fig. 4*B*) and produce EM projections in which they appear laterally closer to the DP than they are.

These precise differential localizations of Aczonin regions, complemented by differential localizations of regions of Bassoon, Munc13, and RIM, are unlikely to result from the unspecific, fixation-induced collapse of Aczonin polypeptides whose native configuration is that of a loose coil or of long vertical or horizontal filaments. Instead, they suggest a more compact native in situ conformation of Aczonin consisting of a “trunk” encompassing the N-terminal 70% of the polypeptide (vertical span, ∼22 nm; horizontal radius ≤10 nm) and sitting on the tip of a DP, and an “arm” extending approximately 22 nm toward the PM and again approximately 22 nm away from the center toward the periphery of the DP (Fig. 4*A*). Along the amino acid sequence, immunogen segments alternate several times between the upper and the lower part of the trunk (*cf*. Fig. 1*A*). Cytomatrix aggregates—which might correspond to Aczonin trunks and associated proteins—on DP-like syndesome tips have also been described by electron tomography (figure 9 of ref. 13). The Aczonin trunk is not quite as compacted as a truly globular protein [e.g., the 410-kDa decamer of glutamine synthetase has a size of 9 × 10 × 10 nm (24)], and may leave interstices between its domains to accommodate binding partners. The molecular determinants that position Aczonin, centered on DPs and at a defined distance from the PM, remain to be identified.

The oligomeric state of Aczonin in situ is unknown. In Fig. 4 *A* and *B*, we depict a homodimeric configuration as one possibility. Monomers, trimers, or hexamers are also conceivable, as are heterooligomers with Bassoon because the Aczonin CC2 domain (between Acz4 and Acz6; Fig. 1*A*) binds strongly to Bassoon (5). With two Aczonin molecules per DP, as assumed in Fig. 4*B*, all docked vesicles in the interior of the grid and half those on the periphery of the grid could interact with one Aczonin arm. Trimers could saturate also most peripheral vesicles.

At the photoreceptor synaptic ribbon, the localizations of the different Aczonin epitopes are indiscriminable, both along the ribbon axis and perpendicular to it (Fig. 3 and Table S1). Also this finding is consistent with a compact conformation of Aczonin molecules, densely occupying the ribbon as demonstrated strikingly by the sensitive antibody anti-Aczp18p19 (Fig. 3*A*). Loose coils of large diameter, or elongated topologies perpendicular or parallel to the ribbon axis, would have produced markedly differential localizations of different sequence regions along these axes. The distances of putative trunk and arm immunogens of Aczonin from the ribbon surface are much closer together (without even a tendency of an N- to C-terminal localization gradient) than at conventional synapses, where they have clearly discriminable localizations vertically and horizontally. Aczonin apparently binds to the ribbon in an orientation that gives a more condensed projection pattern of horizontal epitope positions than at conventional synapses. Different Aczonin topologies may be caused by the molecular environment, which is at least partially different in both locations. Aczonin may even be woven into the matrix of the ribbon, partly or completely. This is suggested in particular by the colocalization of all Aczonin immunogens with CtBP2/Ribeye, a main constituent of the ribbon matrix. Whereas postembedding immunogold EM of CtBP2/Ribeye decorated the ribbon cross-section (25), our preembedding labeling system [which used the same primary antibody used by tom Dieck et al. (25)] did not penetrate into the ribbon matrix and only decorated the space around it (Fig. 3*B*), presumably depending on surface-near epitope position or on epitope exposure by superficial structural disruption. The median distances of Aczonin and CtBP2/Ribeye immunolabel from the ribbon surface are between 10 and 23 nm (Table S1) and can be largely accounted for by the molecular dimensions of the detection system (the diagonal span of a primary IgG molecule is 10–12 nm, and the length of a secondary Fab-nanogold complex is ∼8 nm).

Aczonin Localization at Conventional and Ribbon Synapses Is Consistent with a Role in Vesicle Recruitment.

Topology and positioning of Aczonin at the conventional synapse relates strikingly to the sizes of neurotransmitter vesicles and DPs. The interval of 33 to 39 nm between the PM-proximal C-terminal parts of Aczonin [which include the CC3 region that can form a multidomain complex with CAST1, Munc13, Bassoon, and RIM (5)] and the PM fits one vesicle diameter (determined as 38 nm in our own specimens). Thus, Aczonin and its interaction partners are positioned such that they could control the access of vesicles from the reserve pool in the interior of the terminal to dock at the presynaptic PM and enter the release-ready pool, in a restrictive (i.e., filter-like) or catalytic (i.e., percolator-like) mode. “Filter” and “percolator” functions are not mutually exclusive: vesicles may be recruited by the upper side of the Aczonin layer, but passed on toward the release site only in a restrained fashion. The C-terminal arm of Aczonin, with the CC3, PDZ, and C2 domains or their binding partners, may reach out toward vesicles sideward and downward and could maintain contact with them even in the

docked state or during exocytosis. In cryoelectron tomography of frozen/hydrated conventional synapses, the vesicle density in a layer 45 to 75 nm parallel to the presynaptic PM was reduced to half the densities in the spaces above and below (18). The dimension of this vesicle-depleted layer fits remarkably well with the layer that we find occupied by Aczonin (33–79 nm). Recent studies of neurons deficient for Aczonin/Piccolo alone (26) or in combination with Bassoon (27) both reveal impacts on vesicle clustering, and one of them also suggests that Aczonin may regulate the transit of vesicles from the reserve to the release-ready pool through modulation of Synapsin dynamics (26). Recent functional studies in Bassoon KO mice similarly indicate a role for Bassoon in vesicle replenishment to the release-ready pool (28).

Aczonin and Bassoon are vertebrate-specific, whereas Bruchpilot, a scaffolding protein important for active zone assembly and vesicle tethering in *Drosophila*, is a C-terminally extended derivative of CAST/ELKS. Although Bruchpilot and Aczonin/Bassoon are unrelated in amino acid sequence, the Bruchpilot polypeptide spans a range of approximately 40 to 65 nm vertical to the presynaptic PM of *Drosophila* neuromuscular junctions (23, 29), remarkably similar to the vertical range spanned by Aczonin and Bassoon at mammalian conventional synapses.

At ribbon synapses, the localization of Aczonin all over the ribbon is also consistent with a role in vesicle recruitment, potentially followed by participation in compound fusion or in conduction of vesicles to the PM fusion site. Again, catalytic and restrictive roles in vesicle recruitment are conceivable, corresponding to the “conveyor belt or safety belt” metaphor (30) for the unclear role of the ribbon in vesicle dynamics. Aczonin may also play a structural role in the ribbon matrix, contributing to the organization of the ribbon morphology and its developmental and functional plasticity (12, 31). In this respect, the morphological and functional phenotype of ribbon synapses in Aczonin/Piccolo KO mice will be of interest.

Spatial Relationships Between Aczonin and Its Molecular Interaction Partners.

We focused on determining the localizations of protein domains that are known to interact with the Aczonin CC3 region represented by construct Acz7-6. The central region of CAST1 and the NT region of Munc13-1 bind directly to Aczonin-CC3, whereas the NT region of RIM1 and the CT region of Bassoon interact indirectly via Munc13-NT (5). We find that at conventional synapses, Bassoon-CT localizes remarkably close to Aczonin-CC3 and the C-terminal Aczonin domains (AczC2A, -C2), both vertically and laterally (Fig. 4*A*). As the two proteins have homologous molecular architectures over most of their lengths (Fig. 1*A*) (2), Bassoon as a whole may have a similar in situ topology as Aczonin at least at conventional synapses. In perfusion-fixed and cryo-immunogold–labeled rat hippocampus, Bassoon aa 756–1,001 (immunogen sap7f), a region that is collinear with Aczonin aa 1,350 to 1,650, was mapped to a PM distance of approximately 80 nm (32), consistent with our value of 73 nm for Acz2 (aa 1,226–1,515). Importantly, virtually the same PM distance (~70 nm) was determined for Bassoon-sap7f after cryofixation and postembedding immunogold labeling (16). Hence, the vertical ultrastructural localization of this more N-terminal Bassoon sequence is also very similar to the corresponding Aczonin segment and little affected by the fixation and processing technique. This supports the validity of our own localization data obtained in chemically perfusion-fixed specimens.

By superresolution immunofluorescence microscopy of chemically fixed conventional synapses, Dani et al. (33) determined PM distances for N- and C-terminal sequences of Aczonin and Bassoon (Aczonin aa 600–700, 80 nm; Aczonin aa 4,439–4,776, 37 nm; Bassoon aa 756–1,001, 70 nm; Bassoon aa 3,612–3,942, 40 nm) that are very similar to the corresponding values determined by us and provide further support that Aczonin and Bassoon have similar topologies at conventional synapses. Similar to our results, Dani et al. (33) also observed a closer localization of RIM toward the PM (30 nm; determined for RIM1 aa 596–705).

In contrast to Aczonin-CC3 and Bassoon-CT, we localized their common interaction partner Munc13-NT and the latter's third binding partner RIM-NT (5) significantly closer to the PM of conventional synapses (19 nm by preembedding labeling). This differential localization could be caused by one or several of the following reasons: (*i*) RIM and Munc13 may be present in molar excess over Aczonin and Bassoon at the neurotransmitter release site, the main pools concentrating at 19 nm and only minor subpools binding more distally to Aczonin-CC3 and Bassoon-CT. (*ii*) Immunodetection of free or dimeric Munc13-NT and RIM-NT near the PM may be favored, whereas the immunodecoration of

more distal pools in complex with Aczonin or Bassoon may be masked by these binding partners. (*iii*) Finally, RIM and Munc13 may translocate during presynaptic activity. They may be PM-near in resting synapses, and move away from the PM and engage with Aczonin-CC3 and Bassoon-CT in the course of vesicle exocytosis. This is supported by studies demonstrating depolarization-induced redistribution of RIM (34) and phorbol ester-induced shuttling of Munc13-1 between the PM and the cytosol (35). Activity-dependent movement of Aczonin or Bassoon, particularly of their C-terminal arms, in the opposite direction is also conceivable.

Our finding that aa 865–881 within the large cytoplasmic loop of the $Ca_v2.1$ (P/Q-type) Ca^{2+} channel colocalized at 20 nm PM distance with Munc13-NT and RIM-NT, is interesting with respect to the close functional and molecular connections of this channel with the exocytosis machinery. The epitope recognized by the antibody lies within the "synprint" region, which binds several presynaptic proteins, including RIM1 (36, 37). Regrettably, we could not determine the lateral localization of the Ca^{2+} channel in the DP preparation. Neither could we detect CAST1 in cerebellar synapses, but Siksou et al. (16) localized an N-terminal CAST1 epitope (aa 107–138) close to the PM (peak at ~30 nm) of hippocampal synapses, in a range where we localize the CAST1-binding Munc13-NT (19 nm) and Aczonin-CC3 sequences (37 nm).

Whereas, at conventional synapses, Aczonin is segregated from Munc13, RIM, and possibly CAST1 but colocalizes with Bassoon, the spatial segregation of Aczonin from these active zone proteins is even more pronounced at the ribbon synapse. Here, Aczonin colocalizes with Ribeye over the entire ribbon, whereas Bassoon, CAST1, Munc13, and RIM are detected only near the ribbon base and the putative vesicle fusion site. This suggests more differential roles of Aczonin and Bassoon at ribbon synapses, as opposed to more overlapping roles at conventional synapses. At photoreceptor ribbons, we have mapped the Bassoon CT region (aa 3,601–3,942; BsnH12) to the vicinity of the ribbon base and active zone. The same localization was determined by others for a Bassoon N-terminal sequence (aa 95–210; BSN6.3) (38) and repeatedly for aa 756 to 1,001 or aa 738 to 1,035 (25, 39–41). These data suggest a compact molecular configuration for Bassoon at the ribbon base as well.

Munc13, CAST, and RIM Isoforms at Ribbon Synapses.

We have labeled the vicinity of the base of photoreceptor ribbons with an antibody raised against the Munc13-1 NT region. It was reported earlier that Munc13-1 is absent from the outer plexiform layer of the retina, where the photoreceptor synapses localize (42). As the antibody we applied to ribbon synapses (anti-Mu1-rb2) has a cross-reactivity of 30% with the isoform ubMunc13-2 (Fig. S1*A*), it is possible that the decoration of the ribbon base or active zone with our Munc13 antibody is caused by this cross-reactivity. Our localization of CAST1 (aa 325–677) to the ribbon base or active zone is in agreement with Deguchi-Tawarada et al. (41), in whose work an antibody against CAST1 aa 183 to 308 was used.

Our results are mostly consistent with the differential localizations of proteins at ribbon bodies versus active zones of ribbon synapses that were determined by tom Dieck et al. (25) with different methodology (different antibodies except that for Ribeye; detection of some proteins by postembedding immunogold EM, others by immunofluorescence in Bassoon-KO mice, which display ribbon detachment from the exocytosis site), with one striking exception. Whereas our RIM antibodies, raised against the N-terminal 387 aa of RIM1, labeled only the ribbon base or release site and spared the ribbon body, tom Dieck et al. (25) obtained labeling of the ribbon base and release site with a RIM2 antibody and of the ribbon body with a RIM1 antibody. To clarify this discrepancy, we characterized the isoform and sequence specificities of our antibodies and those of tom Dieck et al. (25) by immunoblot analysis of recombinant proteins (*SI Results* and Fig. S1 *C* and *D*). We found that the commercial RIM1 and RIM2 antibodies used by tom Dieck et al. (25) had substantial mutual cross-reactivity (50–70%) on Western blots, although they appeared to be isoform-specific enough to label differential localizations in the postembedding immunogold EM and immunofluorescence microscopy of tom Dieck et al. (25). They were raised against central sequence regions around the PDZ domains that are present in the α- as well as the β-transcript variants of RIM1 and RIM2. Our own three sera, after subtraction of Rabphilin cross-reactivity, also displayed significant cross-reactivity for RIM2 (25–40%), which may explain their decoration of the ribbon base. Surprisingly, they reacted almost exclusively with the short N-terminal partial sequence of RIM1 (aa 9–55) and probably its counterpart in RIM2, which is essential for Rab3 binding and absent in the β-transcript variants of RIM1 and RIM2 (43). Our antibodies are therefore expected to specifically detect RIM1α and RIM2α. Our

immunolocalization results can be reconciled with those of tom Dieck et al. (25) if RIM2α was the dominant or exclusive isoform at the exocytosis site, whereas the dominant or exclusive isoform on the ribbon body was RIM1β. This would have interesting mechanistic implications, as RIM1β cannot bind Rab3, and its putative role in vesicle recruitment or compound fusion at photoreceptor ribbons would be independent of Rab3. However, a third study of RIM localization at photoreceptor ribbon synapses (41), which used a monoclonal antibody against the RIM1 PDZ domain [aa 602–723; a different antibody against virtually the same immunogen as tom Dieck et al (25)] expected to detect both the α- and β-transcript variants, like us observed labeling of only the ribbon base or exocytosis site and could not confirm the presence of RIM1 on the ribbon body. In light of the findings of tom Dieck et al. (25), they attributed the decoration of the ribbon base to putative (although unproven) cross-reactivity with RIM2 but left the lack of labeling of the ribbon body unexplained (41). Both the detection of RIM1 at the ribbon body and the identification of the RIM isoform at the ribbon base as RIM2 then rest solely on the finding of tom Dieck et al. (25) that their Synaptic Systems RIM1ab1 antibody labeled the ribbon body but not the exocytosis site. Unfortunately, the commercial antibody used by Deguchi-Tawarada et al. (41) (no. 610906; Becton-Dickinson) is no longer available, so we could not include it in our immunoblot analysis of isoform specificity. The presence, localization, molecular nature, and functions of RIM isoforms at ribbon synapses require clarification with additional isoform- and transcript-variant–specific molecular probes and, crucially, in RIM1- and RIM2-KO mice.

Toward an Integration of the Molecular, Ultrastructural, and Functional Anatomy of the Active Zone.

The present study provides insights into the higher levels of organization of the presynaptic molecular machinery. As a step toward correlating the molecular and the ultrastructural architectures of active zones, we have mapped the in situ topology of the Aczonin polypeptide chain and of some of its molecular interaction partners at conventional and ribbon synapses. Our results reveal a nanometer-scale molecular compartmentalization of the active zone of conventional synapses, in the form of vertical stratification and horizontal periodicity, which correlates closely with the physical dimensions of neurotransmitter vesicles and DPs. They confirm the molecular compartmentalization of ribbon synapses that has emerged in recent years but raise questions regarding the presence and localization of RIM isoforms at ribbons.

Materials and methods

Immunogold EM and Morphometry

All experimental procedures conformed to international guidelines of the ethical use of animals and were approved by the German and Swedish animal welfare authorities. Adult Sprague–Dawley rats were deeply anesthetized and fixed by transcardiac perfusion. The blood vessels were briefly flushed with PBS solution containing 0.3% sodium nitroprusside and heparin (10 U/mL) before fixation after two different protocols: (*i*) 4% paraformaldehyde, 0.05% glutaraldehyde, 0.2% picric acid in 0.1 M sodium phosphate buffer (PB), pH 7.4 (PGPic; ref. 44); or (*ii*) 4% paraformaldehyde in 0.1 M sodium acetate buffer, pH 5.6, followed by 4% paraformaldehyde in 0.1 M sodium carbonate buffer, pH 10.8 (PFA pH-shift; ref. 45). Fixation was carried out at room temperature for approximately 20 min at a flow rate of 20 mL/min. Cerebellum and retinas were dissected out, immersed in the fixative agent overnight at 4 °C, and washed thoroughly with PBS solution.

For postembedding immunogold labeling, Vibratome sections (50–100 μm thick) were embedded in Lowicryl resin. Dehydration was done by freeze-substitution or by progressive lowering of temperature dehydration (46). Before freeze-substitution, Vibratome sections were cryoprotected in glycerol (10%, 20%, 30% in 0.1 M PB) and frozen in supercooled propane (−185 °C). Frozen sections were freeze-substituted in acetone (for embedding in Lowicryl K4M) or in 0.1% uranyl acetate in methanol (for embedding in Lowicryl HM20) for 46 h at −90 °C and warmed to −30 °C at a rate of 3 °C/h. Progressive lowering of temperature was done by dehydration of samples in ethanol. The dehydrated samples were infiltrated at −35 °C with mixtures of the respective pure solvents and Lowicryl HM20 or Lowicryl K4M (1:1 and 1:2; 2 h each), and finally with pure resins overnight and for additional 2 h with fresh resin. UV polymerization was done for 2 d at −30 °C and 1 d each at 0 °C and 20 °C. Ultrathin sections were then floated over the following sequence of solutions, at room temperature unless

indicated otherwise: 50 mM glycine in PBS solution; blocking solution (0.5% cold water fish gelatin, 0.5% BSA, 0.01% Tween 20 in PBS solution); primary antibodies in blocking solution (4 °C overnight); blocking solution; secondary antibody (goat anti-rabbit IgG coupled to 10 nm gold; British Biocell) in blocking solution (90 min); blocking solution; PBS solution; 0.25–2.5% glutaraldehyde in PBS solution (30 min); and water. Ultrathin sections were finally contrasted with lead citrate (HM20) or with an adsorptive staining (10) by using a mixture of uranyl acetate and methyl cellulose (K4M). The latter procedure visualizes DPs.

Preembedding immunolabeling was done according to the following protocol using free-floating Vibratome sections of perfusion-fixed cerebellum and hand cross-sections (thickness, ∼0.5 mm) of PGPic-perfused retina. All steps were carried out at room temperature unless indicated otherwise: permeabilization (1% sodium borohydride in PBS solution) for 45 min; washing with PBS solution (three times for 10 min each); blocking with PBS solution, 10% normal goat serum, 0.02% Triton X-100 (PBNT) for 45 to 60 min; incubation with primary antibody diluted in PBNT for 60 h at 4 °C; washing with PBNT (once for 45 min) and PBS solution (three times for 10 min each); blocking with PBS solution, 1% normal goat serum, 0.5% BSA, 0.4% fish gelatin (PBGN) for 45 to 60 min; incubation with secondary antibody (Nanogold-coupled goat anti-rabbit Fab′; Nanoprobes) diluted in PBGN for 20 h at 4 °C; washing with PBGN (once for 45 min) and PBS solution (three times for 10 min each); fixation of bound antibodies with 2.5% glutaraldehyde in 0.1 M PB for 45 min; and washing with PB (twice for 10 min each).

Silver enhancement of Nanogold particles was done following the report of Burry et al. (47). Particles were silver-intensified for 10 to 13 min under red safe light to avoid light-induced silver nucleation. Tissue samples were postfixed with 1% osmium tetroxide in PB for 20 min and washed with PB (twice for 5 min) and water (twice for 5 min). En bloc staining with 0.5% aqueous uranyl acetate was done for 20 min to enhance overall contrast. After washing with water (three times for 5 min each), samples were dehydrated in ethanol (50%, 60%, 70%, 80%, 90%, 95%, 100%, 100% ethanol, 15 min each) and propylene oxide (twice for 10 min, once for 30 min) and infiltrated with Araldite resin (overnight with 1:1 mixture of Araldite and propylene oxide, 4 h pure resin). After embedding in fresh Araldite, the resin was cured overnight at 60 °C. Ultrathin sections were collected on copper grids and counterstained with 3% uranyl acetate in 70% methanol (25–30 min) and with lead citrate (6 min).

When preparing cerebellum samples for studying epitope localization in the horizontal direction of conventional synapses, staining with EPTA (11) was included in the protocol to enhance the visibility of DPs. After dehydration with 95% ethanol, samples were incubated for 1 h with 1% phosphotungstic acid in 100% ethanol containing three drops of 95% ethanol per 10 mL staining solution. The water content of the staining solution was critical for the staining result and had to be adjusted carefully. The heavy metal stain was washed out with cold propylene oxide (1× rinse, two times for 15 min), and samples were infiltrated and embedded in Araldite resin as described earlier.

In case of insufficient immunolabeling, Vibratome (cerebellum) or hand (retina) sections of PGPic-fixed tissues were microwave-treated before the preembedding immunolabeling procedure to allow for heat-induced antigen retrieval (HIAR) (48, 49). Sections were immersed in 15 mL retrieval solution (0.01 M citrate buffer, pH 6.0; 1 mM EDTA-NaOH, pH 8.0; or 20 mM Tris, 40 mM NaCl, pH 9.0) and heated in a household microwave oven at 500 W in short intervals of 30 to 100 s for a total of 5 min. Samples were allowed to cool to room temperature, transferred to PBS solution, and processed for immunolabeling. Microwave treatment in EDTA-NaOH had the strongest effect on antigen retrieval but slightly impaired the ultrastructural appearance of the samples, whereas citrate or Tris buffers did not affect the ultrastructure. Epitope localization was not altered by the microwave treatment in any of the retrieval solutions, as immunolabeling of two different immunogens (Aczp18p19 and Rim43) produced identical results for both microwave-processed and untreated samples (*SI Results*).

For morphometric analysis of epitope localization in cerebellum samples, synapses were selected at random in at least two sections from each experiment if the following criteria were met: (*i*) synaptic complex exhibits enhanced electron density and unilateral vesicle clustering; (*ii*) plane of sectioning is perpendicular to the pre- and postsynaptic PMs, i.e., membranes are clearly visible and run parallel; (*iii*) at least one labeling particle is present; and (*iv*) individual particles are separable (i.e., no extensive fusion of particles as a result of silver intensification). As membranes were hardly visible in samples stained with EPTA, the proper plane of sectioning was indicated by a regular array of dense projections at the presynaptic site. The morphological criteria for the selection of photoreceptor ribbon synapses in the outer plexiform layer of the retina were (*i*) the characteristic triad shape of

postsynaptic elements made up by horizontal and bipolar cell dendrites and (*ii*) the characteristic arrangement of presynaptic structures, i.e., synaptic ribbon and arciform density. Measurements were done on digitally recorded EM images or on high-resolution scans of negatives by using a customized version of the National Institutes of Health Image program Image SXM (version 1.62) or CorelDRAW X3. At conventional synapses, epitope localization in the vertical direction was determined by measuring the distance of particles perpendicular to the PM. For the determination of epitope localization in horizontal direction, the shortest distance to the virtual midline of the nearest DP was measured in samples stained with EPTA. At photoreceptor ribbon synapses, particle distances were measured horizontally to the surface of the ribbon and vertically to the base point of the presynaptic PM. As silver intensification yields asymmetric particles, the shortest and longest distances of the circumference of a particle were measured, and the mean distance calculated from these values. For descriptive statistics the median (i.e., 50th percentile) and the 95% CI were calculated. Distributions were compared pairwise with a nonparametric test according to Kolmogorov and Smirnoff (ref. 50, or other standard literature on statistics). We used nonparametric statistics because not all distributions were normal distributions. The Kolmogorov–Smirnoff test is one of the sharpest nonparametric tests for homogeneity (50).

Expression Constructs and Antibodies

Partial cDNA sequences were amplified from mouse brain RNA by RT-PCR and inserted into the SmaI sites of the RGS-His-tag vector pQE32 (Qiagen), the GST vector pGEX-4T-2 (GE Healthcare), or the thioredoxin vector pBAD/Thio-TOPO (Mu1; Invitrogen). Immunogen sequence regions are shown in Table 1 and in the overview of Fig. 1*A*. Recombinant proteins were expressed in bacteria and used for the immunization of rabbits and guinea pigs. Sera were affinity-purified on the same recombinant proteins used for immunization. Sequence regions Acz6 and Acz7-6 have partial similarity with the collinear regions of Bassoon; their antibodies were therefore subtracted with the corresponding Bassoon fusion proteins, and specificities after subtraction were confirmed with Western blots of the recombinant Aczonin/Bassoon proteins. All other Aczonin antigen sequences have no or minor sequence similarity with Bassoon, and the respective antibodies gave typical Aczonin band patterns on Western blots of brain lysate. An affinity-purified rabbit antibody against aa 865 to 881 (accession no. P54282) of the rat P/Q-type calcium channel α1A subunit was from Chemicon (AB5152). A monoclonal antibody against CtBP2/Ribeye was from BD Biosciences (no. 612044). The RIM1/2, Aczonin, and Rabphilin constructs used for immunoblotting (Fig. S1 *C* and *D*) were cloned into the SmaI site of pQE32 and carried an N-terminal RGS-His tag. The Munc13-1(1-320) and ubMunc13-2(1-345) constructs for immunoblotting (Fig. S1*A*) were cloned into a derivative of pET3 (Novagen) engineered in our laboratory such that the recombinant protein begins with its natural start codon and carries a C-terminal His-tag. C-terminally His-tagged fusion proteins were detected with anti-His(C-term) monoclonal antibody (R930-25; Invitrogen) and N-terminally His-tagged fusion proteins with anti-RGS-His monoclonal (no. 34610; Qiagen). Construct Rim1(207–366) was cloned at Synaptic Systems into a derivative of pASK-IBA37plus (IBA) and carries an N-terminal RGS-His-tag; it expresses the immunogen used at Synaptic Systems to generate a new RIM1-specific antibody (RIM1ab2, no. 140 013) and was provided by Henrik Martens (Synaptic Systems, Göttingen, Germany). All our own antibodies were affinity-purified rabbit antisera, except anti-Aczp2p4, which was a crude guinea pig serum. Vertical localization at conventional synapses was analyzed with two independent sera for AczN, Aczp18p19, AczC2, and Mu1, and with three sera for Rim43, with concordant results for each immunogen, which were pooled to determine the quantitative parameters in Fig. 1. After having confirmed for several immunogens the reproducibility of localizations obtained with independent antisera, and additionally for the three closely adjacent or overlapping Bassoon C-terminal sequences, other localizations were determined with one serum per immunogen.

Supplementary Material

http://www.ncbi.nlm.nih.gov/pmc/articles/PMC3150911/bin/supp_108_31_E392__index.html

Acknowledgments

We thank Prof. Karl Meller for support in the early stages of this work, Dr. Ruth Dahlen for her help with the morphometry of dense projections, and Dr. Henrik Martens for the RIM1α(207–366) expression construct. This work was supported by Deutsche Forschungsgemeinschaft Grant Ki 324/13, Fonds der Chemischen Industrie, the intramural research funding program (FoRUM) of the University of Bochum Medical School, and start-up funds from the Faculty of Science and Technology of Uppsala University, all to M.W.K. N.T. was supported by a fellowship from the LEONARDO Program of the European Union.

Conflict of Interest

The authors declare no conflict of interest.

References

1. Wojcik SM, Brose N (2007) Regulation of membrane fusion in synaptic excitationsecretion coupling: speed and accuracy matter. Neuron 55:11–24.
2. Schoch S, Gundelfinger ED (2006) Molecular organization of the presynaptic active zone. Cell Tissue Res 326:379–391.
3. Phillips GR, et al. (2001) The presynaptic particle web: Ultrastructure, composition, dissolution, and reconstitution. Neuron 32:63–77.
4. Zhai RG, Bellen HJ (2004) The architecture of the active zone in the presynaptic nerve terminal. Physiology (Bethesda) 19:262–270.
5. Wang X, et al. (2009) A protein interaction node at the neurotransmitter release site: Domains of Aczonin/Piccolo, Bassoon, CAST, and RIM converge on the N-terminal domain of Munc13-1. J Neurosci 29:12584–12596.
6. Wang X, et al. (1999) Aczonin, a 550-kD putative scaffolding protein of presynaptic active zones, shares homology regions with RIM and Bassoon and binds profilin. J Cell Biol 147:151–162.
7. Fenster SD, et al. (2000) Piccolo, a presynaptic zinc finger protein structurally related to bassoon. Neuron 25:203–214.
8. Jin Y, Garner CC (2008) Molecular mechanisms of presynaptic differentiation. Annu Rev Cell Dev Biol 24:237–262.
9. Kaeser PS, et al. (2009) ELKS2α/CAST deletion selectively increases neurotransmitter release at inhibitory synapses. Neuron 64:227–239.
10. Roth J, Taatjes DJ, Tokuyasu KT (1990) Contrasting of Lowicryl K4M thin sections. Histochemistry 95:123–136.
11. Bloom FE, Aghajanian GK (1968) Fine structural and cytochemical analysis of the staining of synaptic junctions with phosphotungstic acid. J Ultrastruct Res 22:361–375.
12. Spiwoks-Becker I, Glas M, Lasarzik I, Vollrath L (2004) Mouse photoreceptor synaptic ribbons lose and regain material in response to illumination changes. Eur J Neurosci 19:1559–1571.
13. Zampighi GA, et al. (2008) Conical electron tomography of a chemical synapse: Polyhedral cages dock vesicles to the active zone. J Neurosci 28:4151–4160.
14. Harlow ML, Ress D, Stoschek A, Marshall RM, McMahan UJ (2001) The architecture of active zone material at the frog's neuromuscular junction. Nature 409:479–484.
15. Nagwaney S, et al. (2009) Macromolecular connections of active zone material to docked synaptic vesicles and presynaptic membrane at neuromuscular junctions of mouse. J Comp Neurol 513:457–468.
16. Siksou L, et al. (2007) Three-dimensional architecture of presynaptic terminal cytomatrix. J Neurosci 27:6868–6877.
17. Siksou L, Triller A, Marty S (2009) An emerging view of presynaptic structure from electron microscopic studies. J Neurochem 108:1336–1342.
18. Fernández-Busnadiego R, et al. (2010) Quantitative analysis of the native presynaptic cytomatrix by cryoelectron tomography. J Cell Biol 188:145–156.
19. Landis DMD, Hall AK, Weinstein LA, Reese TS (1988) The organization of cytoplasm at the presynaptic active zone of a central nervous system synapse. Neuron 1:201–209.
20. Hirokawa N, Sobue K, Kanda K, Harada A, Yorifuji H (1989) The cytoskeletal architecture of the presynaptic terminal and molecular structure of synapsin 1. J Cell Biol 108:111–126.
21. Gotow T, Miyaguchi K, Hashimoto PH (1991) Cytoplasmic architecture of the axon terminal: Filamentous strands specifically associated with synaptic vesicles. Neuroscience 40:587–598.
22. Harris JR, Horne R (1991) Negative staining. Electron Microscopy in Biology: A Practical Approach, eds Harris JR, Horne R (IRL Press, Oxford), pp 203–232.
23. Fouquet W, et al. (2009) Maturation of active zone assembly by Drosophila Bruchpilot. J Cell Biol 186:129–145.
24. Krajewski WW, et al. (2008) Crystal structures of mammalian glutamine synthetases illustrate substrate-induced conformational changes and provide opportunities for drug and herbicide design. J Mol Biol 375:217–228.
25. tom Dieck S, et al. (2005) Molecular dissection of the photoreceptor ribbon synapse: physical interaction of Bassoon and RIBEYE is essential for the assembly of the ribbon complex. J Cell Biol 168:825–836.
26. Leal-Ortiz S, et al. (2008) Piccolo modulation of Synapsin1a dynamics regulates synaptic vesicle exocytosis. J Cell Biol 181:831–846.
27. Mukherjee K, et al. (2010) Piccolo and bassoon maintain synaptic vesicle clustering without directly participating in vesicle exocytosis. Proc Natl Acad Sci USA 107: 6504–6509.

28. Hallermann S, et al. (2010) Bassoon speeds vesicle reloading at a central excitatory synapse. Neuron 68:710–723.
29. Hallermann S, et al. (2010) Naked dense bodies provoke depression. J Neurosci 30: 14340–14345.
30. Parsons TD, Sterling P (2003) Synaptic ribbon. Conveyor belt or safety belt? Neuron 37:379–382.
31. Regus-Leidig H, Tom Dieck S, Specht D, Meyer L, Brandstätter JH (2009) Early steps in the assembly of photoreceptor ribbon synapses in the mouse retina: The involvement of precursor spheres. J Comp Neurol 512:814–824.
32. Sanmartí-Vila L, et al. (2000) Membrane association of presynaptic cytomatrix protein bassoon. Biochem Biophys Res Commun 275:43–46.
33. Dani A, Huang B, Bergan J, Dulac C, Zhuang X (2010) Superresolution imaging of chemical synapses in the brain. Neuron 68:843–856.
34. Tao-Cheng JH (2006) Activity-related redistribution of presynaptic proteins at the active zone. Neuroscience 141:1217–1224.
35. Betz A, et al. (1998) Munc13-1 is a presynaptic phorbol ester receptor that enhances neurotransmitter release. Neuron 21:123–136.
36. Coppola T, et al. (2001) Direct interaction of the Rab3 effector RIM with Ca2+ channels, SNAP-25, and synaptotagmin. J Biol Chem 276:32756–32762.
37. Evans RM, Zamponi GW (2006) Presynaptic Ca2+ channels—integration centers for neuronal signaling pathways. Trends Neurosci 29:617–624.
38. Dick O, et al. (2003) The presynaptic active zone protein bassoon is essential for photoreceptor ribbon synapse formation in the retina. Neuron 37:775–786.
39. Brandstätter JH, Fletcher EL, Garner CC, Gundelfinger ED, Wässle H (1999) Differential expression of the presynaptic cytomatrix protein bassoon among ribbon synapses in the mammalian retina. Eur J Neurosci 11:3683–3693.
40. Dick O, et al. (2001) Localization of the presynaptic cytomatrix protein Piccolo at ribbon and conventional synapses in the rat retina: Comparison with Bassoon. J Comp Neurol 439:224–234.
41. Deguchi-Tawarada M, et al. (2006) Active zone protein CAST is a component of conventional and ribbon synapses in mouse retina. J Comp Neurol 495:480–496.
42. Schmitz F, Augustin I, Brose N (2001) The synaptic vesicle priming protein Munc13-1 is absent from tonically active ribbon synapses of the rat retina. Brain Res 895:258–263.
43. Kaeser PS, et al. (2008) RIM1α and RIM1β are synthesized from distinct promoters of the RIM1 gene to mediate differential but overlapping synaptic functions. J Neurosci 28:13435–13447.
44. Somogyi P, Takagi H (1982) A note on the use of picric acid-paraformaldehydeglutaraldehyde fixative for correlated light and electron microscopic immunocytochemistry. Neuroscience 7:1779–1783.
45. Berod A, Hartman BK, Pujol JF (1981) Importance of fixation in immunohistochemistry: Use of formaldehyde solutions at variable pH for the localization of tyrosine hydroxylase. J Histochem Cytochem 29:844–850.
46. Acetarin JD, Carlemalm E, Villiger W (1986) Developments of new Lowicryl resins for embedding biological specimens at even lower temperatures. J Microsc 143:81–88.
47. Burry RW, Vandré DD, Hayes DM (1992) Silver enhancement of gold antibody probes in pre-embedding electron microscopic immunocytochemistry. J Histochem Cytochem 40:1849–1856.
48. Shi SR, Key ME, Kalra KL (1991) Antigen retrieval in formalin-fixed, paraffinembedded tissues: An enhancement method for immunohistochemical staining based on microwave oven heating of tissue sections. J Histochem Cytochem 39: 741–748.
49. Yamashita S (2007) Heat-induced antigen retrieval: Mechanisms and application to histochemistry. Prog Histochem Cytochem 41:141–200.
50. Sachs L (1982) Applied Statistics (Springer Verlag, New York).

Tables and Figures

Table 1. Immunogen sequences

Designation	Sequence interval	Terminal aa
AczN	63–218	LPK…IPK
Aczp2p4	486–755	PTS…SKD
Acz2	1,226–1,515	QPQ…HRR
Aczp18p19	1,808–2,150	QKE…GVS
Acz3	2,521–2,812	TVF…MDE
Acz4	2,784–3,073	STI…TLP
Acz6	3,321–3,604	QYD…GFT
Acz7-6/CC3	3,593–3,784	SRA…PYT
Acz8	3,842–4,121	PTP…SSS
AczC2A	4,566–4,744	PGS…QQS
AczC2	4,725–4,828	EQT…IQP
BsnH12/CT	3,601–3,942	SDR…SFW
BsnH12-3	3,820–3,942	PTT…SFW
BsnH12-7	3,601–3,820	SDR…SQP
Cast3	325–677	DNE…KEE
Rim43/NT	9–387Δ83–105	GPR…RYP
Mu1/NT	2–320	SLL…QDE

Reference sequences: Aczonin (accession no. Y19185), Bassoon (accession no. NM007567), CAST1 (accession no. AY356532), Munc13-1 (accession no. AY753536), and RIM1 (accession no. AJ310531).

Table 2. Lateral immunogen localizations at conventional synapses

		Median lateral distance from DP axis (nm)	
Immunogen	*n*[‡]	Bilateral evaluation (M)	Unilateral evaluation (M*)
Monomodal (centered) distributions			
AczN	254	2 (−2 to 5)	14 (12–16)
Acz2	204	−3 (−6 to 2)	14 (11–17)
Aczp18p19	247	−5 (−8 to −1)	15 (14–18)
Acz3	341	1 (−3 to 3)	14 (12–15)
Bimodal (lateralized) distributions			
Acz8	232	−1 (−7 to 6)	16 (15–18)
AczC2A	220	3 (−7 to 11)	22 (19–23)
AczC2	221	3 (−11 to 12)	22 (21–24)
BsnH12-3	189	5 (−5 to 11)	18 (16–20)
Mu1	233	3 (−8 to 12)	23 (21–27)
Rim43	293	4 (−8 to 11)	22 (20–24)

Values in parentheses are 95% CIs. Bilateral and unilateral evaluation are described in *Results*.

[†]Number of immunolabeling particles.

Figure 1. Stratified presynaptic localizations of sequence regions of Aczonin, Bassoon, Munc13, and RIM in conventional mammalian synapses. (*A*) Domain architectures of Aczonin, Bassoon, Munc13-1, RIM1, and CAST1, and sequence positions of the immunogens used in this study (Table 1). (*B*) Typical overview of preembedding silver-enhanced immunogold EM in the molecular layer of the rat cerebellum with Aczonin antibody anti-Aczp18p19 shows narrow bands of immunodecoration parallel to presynaptic PMs. Synapses sectioned vertically to the PM are marked by arrowheads. Synapses sectioned obliquely or almost parallel to the PM (arrows) can also be seen. (Scale bar: 500 nm.) (*C*) Six regions within the N-terminal 70% of the Aczonin sequence localize to distances of 57 to 79 nm from the presynaptic PM. *Top*: EM image representing this localization (anti-Aczp2p4). Column diagrams with the morphometric data of the six regions are shown below. For each dataset, the median PM distance in nm ("M"), the 95% CI in brackets, and the number of particles evaluated ("n") are indicated. (Scale bars: 100 nm.) (*D* and *E*) Five regions within the C-terminal 30% of the Aczonin sequence and three regions in the C-terminal 10% of the Bassoon sequence localize to distances of 33 to 39 nm from the presynaptic PM. (*F*) The N-terminal 320 aa of Munc13-1/ubMunc13-2 (anti-Mu1), the N-terminal Rab3-binding sequences of RIM1/2α (anti-Rim43), and (*G*) a peptide sequence (aa 865–881) in the large central cytoplasmic loop of the P/Q-type Ca^{2+} channel α1A subunit localize to distances of 19 to 20 nm from the presynaptic PM. (*H*) Direct correlation between Aczonin localization and the physical dimensions of DPs. Sections of Lowicryl K4M-embedded samples subjected to adsorption staining with uranyl acetate/methyl cellulose displayed the regular array of DPs (*Top Left*). When these specimens were postembedding immunolabeled with anti-Aczp18p19 (*Bottom Left*; "post"), gold particles (arrows) were found right above the tips of DPs. The EM image (*Bottom Right*; "pre") shows a synapse decorated with anti-Aczp18p19 by the preembedding technique as in *B*–*G*. Note the negative membrane contrast in the Lowicryl-embedded samples.

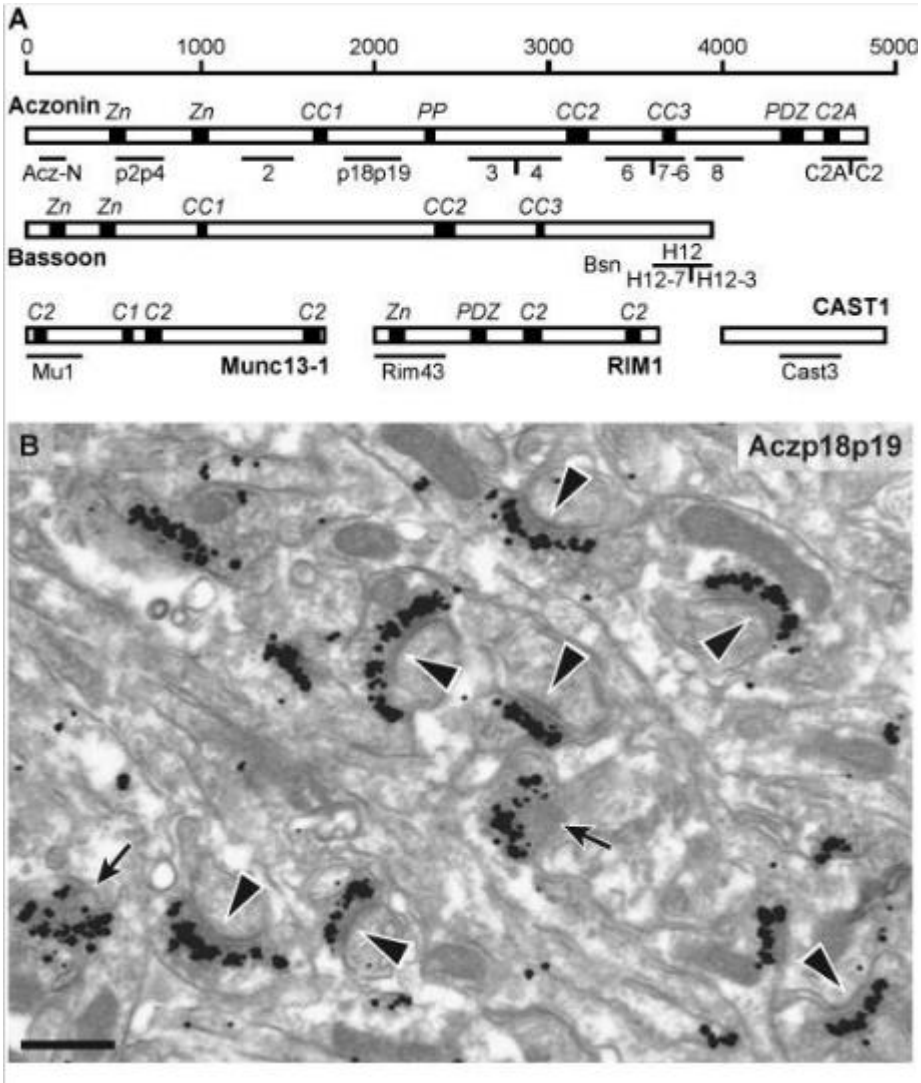

Figure 1 *(continued)*

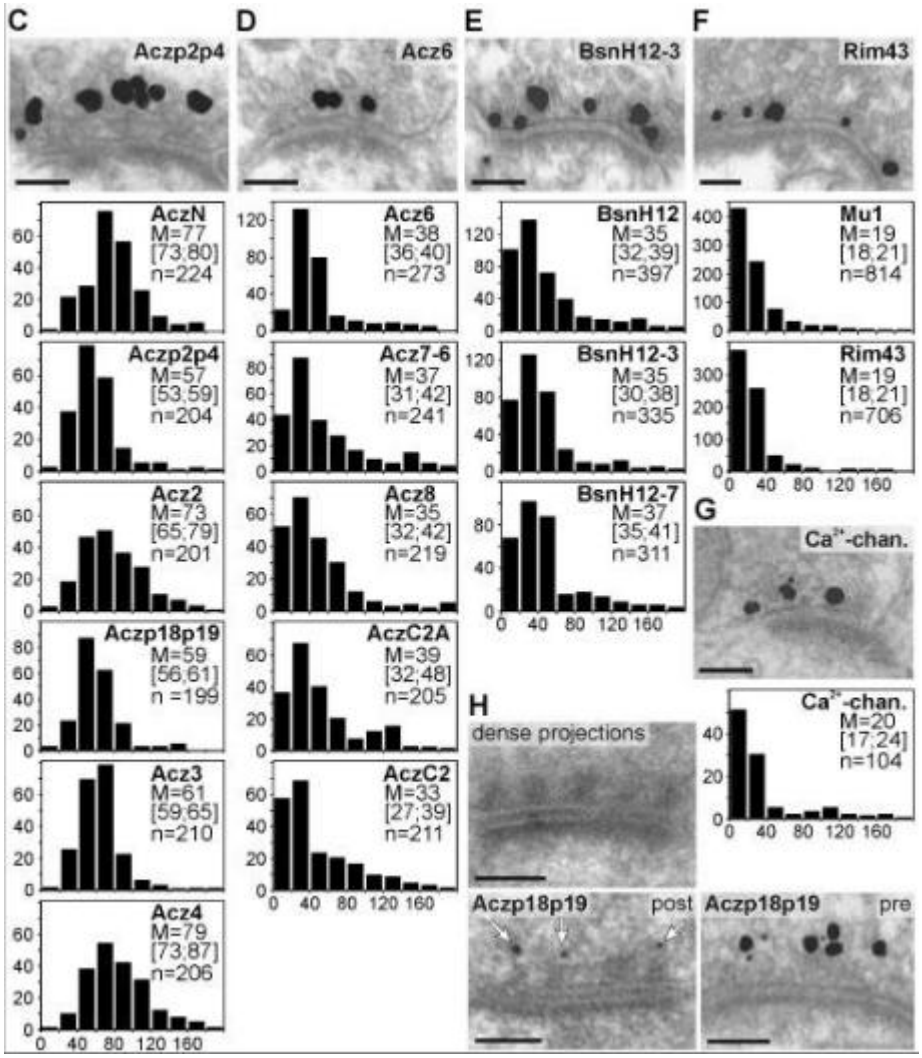

Figure 2 Lateral topology of Aczonin and its interactor protein domains relative to DPs. DPs were visualized by EPTA staining, followed by preembedding immunogold labeling. (*A*) Four immunogens within the N-terminal 70% of the Aczonin sequence localize close to the DP axis. *Top*: Typical EM image (PM-vertical section; white arrowheads point to DPs). Column diagrams with the morphometric data are shown below. In the background of the diagrams, the lateral dimensions of DPs are indicated by a symbolic DP shape and three vertical dashed lines (DP center, 0 nm; width at base, ±28 nm). (*B*) Three immunogens within the C-terminal 30% of the Aczonin sequence localize to the DP periphery. (*C*) The Bassoon CT region and the Munc13 and RIM NT sequences localize to the DP periphery. For *A–C*, *Results* includes information regarding determination and interpretation of the median and M* median values, and Table 2 provides a complete list of morphometric parameters. (*D*) A PM-parallel section of a specimen immunolabeled with anti-Rim43 illustrates that immunodecoration particles (arrows) lie at the sides of DPs. (*E*) An oblique section of an anti-Aczp18p19–labeled specimen illustrates that this immunogen lies above the DP layer. From bottom to top, one sees contiguous electron-dense material representing the postsynaptic density followed by spots representing DPs (arrowheads); as DPs expire further up, immunolabeling particles appear (arrows). (Scale bars: 100 nm.)

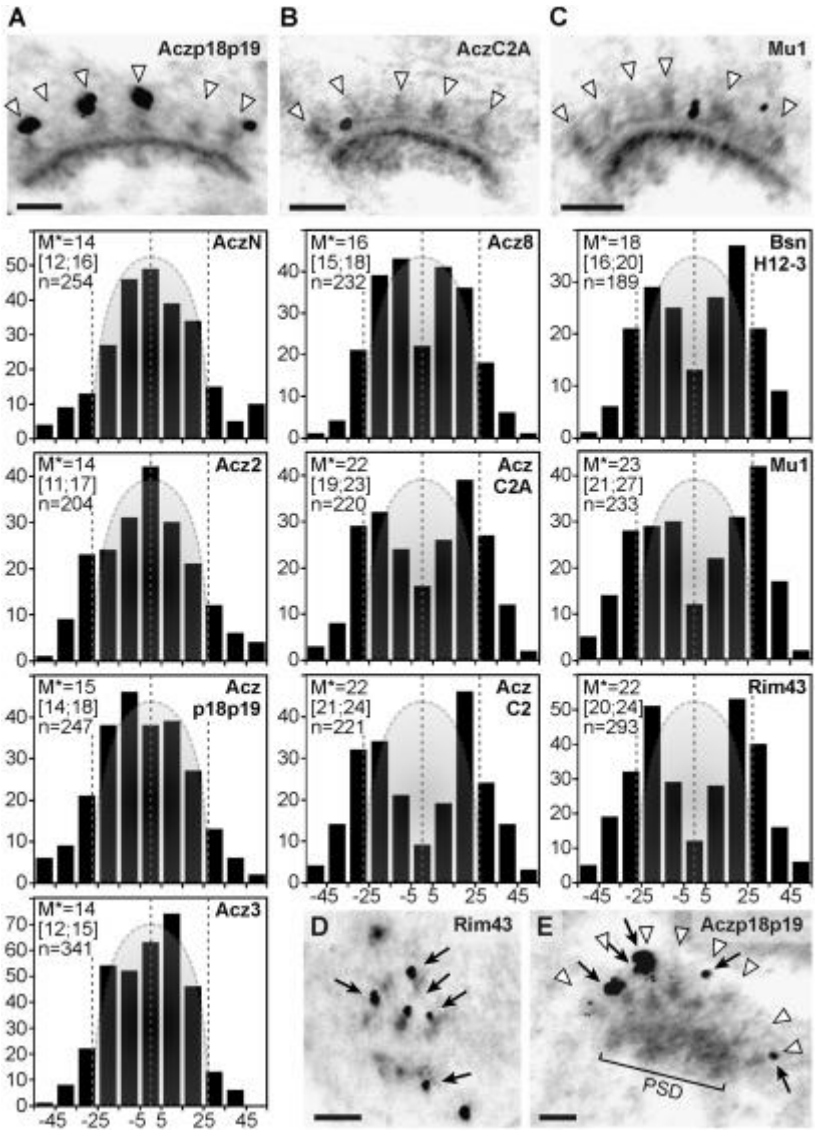

Figure 3 Differential localizations of Aczonin and CtBP2/Ribeye versus Bassoon, CAST1, Munc13, and RIM at photoreceptor ribbon synapses. (*A*) Aczonin (anti-Aczp18p19) is detected over the whole surface of ribbons, in vertical (*Left*) and horizontal sections (*Middle*), and of ribbon precursor spheres (*Right*). (*B*) Antibodies against nine Aczonin sequence regions and against CtBP2/Ribeye produce indiscriminable labeling patterns of the entire ribbon height. *Left*: Organization of ribbon synapse illustrated schematically, aligned to 10 column diagrams that show the morphometric evaluation of the vertical distributions of immunolabel for the different Aczonin regions and CtBP2/Ribeye. Distribution diagrams show the distances of particles from the PM ridge, normalized to the distance between the PM ridge (ordinate position, 0) and the ribbon tip (ordinate position, 1) of the respective synapse. The mean ordinate position of the ribbon base was 0.23. *Right*: Two representative EM images are shown. (*C*) The CT region of Bassoon, the NT sequence of RIM1/2α, the NT region of Munc13, and the central region of CAST1 localize to the ribbon base and/or the vesicle release site. Column diagrams for the vertical distributions of the four immunogens, and three representative EM images are shown. (Scale bars: 100 nm.) Table S1 provides a complete list of the morphometric and statistical parameters of the vertical and horizontal distributions.

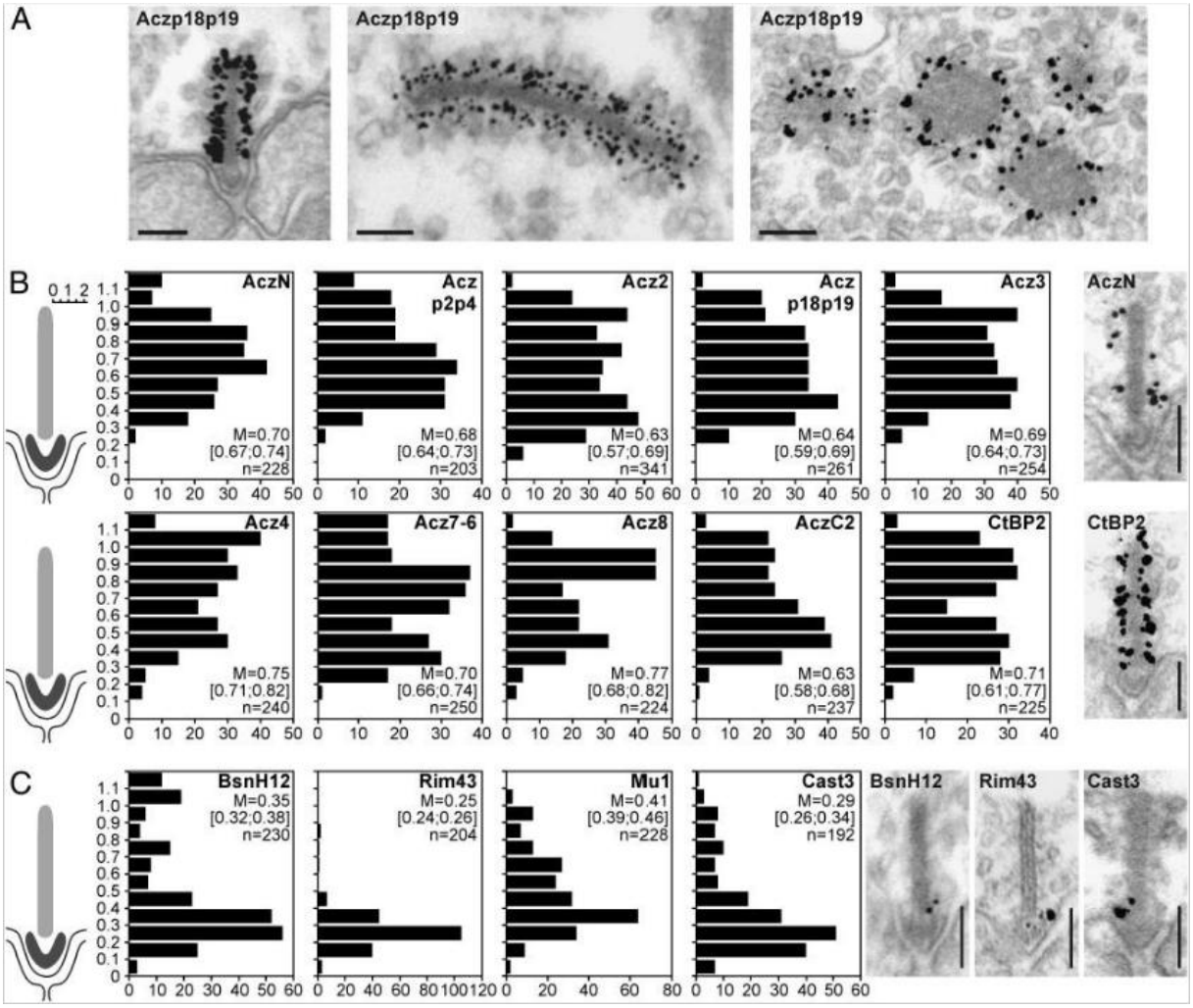

Figure 4 Models for molecular topologies at DPs and the presynaptic particle grid. (*A*) Localizations of Aczonin, Bassoon, RIM, Munc13, and $Ca_v2.1$ calcium channel sequences are indicated in relation to the dimensions of DPs, synaptic vesicles (SV), and the PM as viewed from the side. Vertical and lateral localizations are combined from the results of Figs. 1 and and2.2. Approximate confidence intervals for the localizations, indicated by circular areas around the median values shown as crosses, are uniformly given as 10 nm for simplicity whereas the actual 95% CIs vary between 3 nm and 16 nm in the vertical direction and between 3 nm and 8 nm in the horizontal direction. White horizontal bars show localizations of immunogens for which only the vertical position could be determined; for such Aczonin sequences, the horizontal placements were interpolated from those of neighboring sequences, whereas the horizontal placement of the Ca^{2+} channel epitope is arbitrary. The approximate outline of the Aczonin protein in situ is indicated by a dark green silhouette of 20 nm horizontal diameter. This accounts for possible deviations of unmapped sequence intervals, and for finite true lateral localizations of the DP axis-near immunogens (presumably ≤5 nm but depicted here as zero for simplicity), which are obscured by the inaccuracy of the detection technique of approximately ±10 nm. (*B*) Model of a possible topology of Aczonin within the presynaptic particle grid. An idealized grid is shown as viewed from above, with DPs of 56 nm diameter at base and 72 nm center-to-center distance, and docked synaptic vesicles of 38 nm diameter (values determined in this study). As in *A*, Aczonin molecules are depicted as dimers centered on DPs. (Scale bar: 70 nm as the typical thickness of an ultrathin section for EM.)